Exploring the Phase Space of Zn$_2$SbN$_3$, a Novel Semiconducting Nitride

Journal Name

Exploring the Phase Space of Zn_2SbN_3, a Novel Semiconducting Nitride[†]

Allison Mis,[a,b*] Stephan Lany,[b] Geoff L. Brennecka,[a] and Adele Tamboli[a,b‡]

The novel semiconductor Zn_2SbN_3 is one of a growing list of ternary nitrides with promise for optoelectronic and energy applications. Previous work by Arca *et al.* [*Materials Horizons*, 2019, 6, 1669-1974] first reported synthesis of this material, but did not explore the effects of growth conditions on material formation. In this work, we present a semi-automated study of the relationship between growth conditions and crystallinity *via* high-throughput RF sputtering and a custom X-Ray diffraction analysis routine. Zn_2SbN_3 is found to crystallize in a wide range of growth conditions, and the formation of several contaminant phases is examined. Electron microscopy of these secondary phases, caused both by off-stoichiometry and by growth conditions, provides insight into the growth mechanisms of Zn_2SbN_3. Computational work relates this material to other Zn-based ternary nitrides and offers an explanation for the difficulty of growing cation-ordered material despite the wide range of growth conditions explored.

Multinary nitrides are a fast-growing area of interest for novel optoelectronic materials. They may provide lower-cost, earth-abundant, or non-toxic alternatives to III-V materials, or their novel lattice parameter/bandgap pairings may make them suitable for integration into existing devices like multi-junction solar cells and light-emitting diodes.[1] Multinary nitrides have the additional advantage of the potential for bandgap tuning using cation site disorder or off-stoichiometry.[2,3]

A recent computational study[4] predicted the stability or metastability of over 200 new ternary nitride compounds. This is a vast, unexplored materials space that is well-served by the rapidity of high-throughput synthesis and characterization.

One of these new materials, Zn_2SbN_3, has potential for use in photovoltaic and hydrogen evolution reaction (HER) applications: computations predict a low electron effective mass ($0.15m_e$ in plane and $0.19m_e$ out of plane) and a direct bandgap of 1.71 eV.[5] This material is predicted to have a wurtzite unit cell; a diagram of the cation-disordered cell is shown in Figure 1.

The first report of the synthesis of Zn_2SbN_3[5] demonstrated thin-film growth *via* radio-frequency (RF) sputtering and showed room-temperature photoluminesence with a band gap of 1.55 eV, demonstrating a high-degree of photoactivity even though this material had oxygen contamination upwards of 8% on the anion site. The lower-than-expected band gap is likely due to cation

disorder in the material, as no signs of order were present. Arca's work showed that the conduction band minimum of this material is well-aligned for HER reactions. Additionally, Arca's was the first report of a crystalline antimony nitride in which antimony assumes a positive (+5) oxidation state.

More study of Zn_2SbN_3 is warranted by Arca's preliminary results. Specifically, the relationship between growth conditions and material quality is not well-explored for such a new material. The necessity of mapping the growth conditions and stoichiometry that result in crystalline material is common to the many emerging materials described above. In this work, we present a semi-automated analysis method that adds to existing high-throughput methodology by expediting the interpretation of samples as crystalline or not, using Zn_2SbN_3 as a test material system.

Zn_2SbN_3 also warrants study deeper than high-throughput mapping can provide: it is predicted to be metastable, that is, an elevated nitrogen chemical potential is required for this material to form. A theoretical phase diagram of the Zn-Sb-N space can be found in the SI of reference 5. Previous samples of this material were grown *via* RF co-sputtering without any intentional activation of the nitrogen in the growth chamber. Sputter growth is a highly-energetic process in which a variety of growth parameters interact and likely raise μ_N unintentionally. However, activated nitrogen sources can be used during growth to intentionally elevate μ_N in a more controlled manner, thus making the target phase more energetically favorable and potentially decreasing unwanted effects such as oxygen incorporation.

Given the property tuning available through off-stoichiometry in other multinary nitrides,[6,7] it is also essential to determine the off-stoichiometric behavior of Zn_2SbN_3. Understanding the ef-

[a] *Colorado School of Mines, 1500 Illinois St, Golden, CO, 80401, USA.*
[b] *National Renewable Energy Laboratory, 15013 Denver W Pkwy, Golden, CO, 80401 USA.*
* amis@mines.edu
‡adele.tamboli@nrel.gov
† Electronic Supplementary Information (ESI) available: see attached SI

fects of off-stoichiometry and growth parameters, including the role of nitrogen activation, on film quality is essential to moving Zn_2SbN_3 toward device applications.

In this work, the growth space of Zn_2SbN_3 was further explored through combinatorial RF sputtering growth. A new automated approach to evaluating crystallinity and identifying phases was developed to standardize and expedite the analysis of the large amounts of data collected through the combinatorial approach. This enabled rapid exploration of a wide variety of growth conditions, and more focused study with cross-sectional electron microscopy yielded insight into this novel semiconductor's formation, dependence on μ_N, off-stoichiometric behavior, and potential for cation ordering.

1 Methods

Growth and Characterization

Films were grown through RF co-sputtering in an AJA sputter chamber with a base pressure <5e-8 torr on 2x2" p-Si substrates with 100nm thermal SiO_2. The elemental zinc and antimony sputter sources were angled with respect to each other to produce an intentional cation composition gradient laterally across the film. Activated nitrogen was supplied by an electron cyclotron resonance (ECR) nitrogen plasma source operated at 150 W with a current of 18 A for all films, unless otherwise noted.

Spatially-resolved characterization was performed using the existing suite of combinatorial characterization tools at the National Renewable Energy Laboratory. The films were measured in a 4x11 grid, with 11 equally-spaced columns spanning the composition gradient and 4 equally-spaced rows spanning perpendicular to the gradient. A full substrate (containing a range of compositions) is referred to as a "library," while one point on that library (a single composition) is referred to as a "sample." Data handling and organization was done using COMBIgor, an open-source package for Igor pro.[8]

Cation composition was determined using an automated mapping routine on a Fisher XDV-SDD X-Ray Fluorescence (XRF) spectrometer using Rh L-series excitation. X-ray diffraction (XRD) patterns were collected on a Bruker D8 Discover equipped with an area detector using Cu_{K_α} radiation. Intensity counts were integrated across χ to generate the 1D scans used for analysis. Synchrotron XRD patterns were obtained using the SSRL beamline 1–5, a high-throughput beamline with spatial mapping capabilities.

Cell parameters were calculated by employing a Pawley refinement of the Bruker XRD patterns in *GSAS-II*.[9] Error values shown are the reported errors from the fits.

Scanning transmission electron micrographs were taken on an FEI Talos F200X at 200 keV with a camera length of 77mm. Elemental mapping data were collected using a Super-X Energy Dispersive X-ray Spectroscopy (EDS) system and analyzed with Bruker Esprit 1.9; 1σ error values were used to determine composition measurement uncertainties. Cross-sectional TEM samples were prepared on a FEI Helios Nanolab 600i FIB/SEM with a 2kV cleaning pass to remove surface Ga contamination.

First Principles Calculations

Using the 7 lowest energy structures of Zn_2SbN_3 from the unconstrained structure sampling of a previous work,[4] we performed total energy and electronic structure calculations. In the present work, the relaxed atomic geometries and resulting total energies were obtained with the SCAN functional,[10] which improves the description of lattice parameters compared to standard density functionals. Crystallographic information files (cif) of these structures were generated with the FINDSYM code[11] and are available in the supplementary materials. All first principles calculations were performed with the VASP code.[12,13] The electronic structure was calculated using the single-shot hybrid approach with additional onsite potentials (SSH+V).[14,15] Fitting of the parameters to a GW reference calculation[5] resulted in $\alpha = 0.17$ for the fraction of Fock exchange, in conjunction with V_{Zn-d} = -1.5 eV (approximately equivalent to U = 3 eV) and V_{Sb-s} = +1.0 eV. The SSH+V calculations closely mimic the result of GW and provide a computationally efficient way for band-gap-corrected electronic structure prediction. Note, however, that the gap of the Zn_2SbN_3 ground state comes out slightly larger (1.78 eV) than in the GW reference (1.71 eV),[5] mainly due to the smaller SCAN lattice constant compared to the reference calculation.

Implementing an Automated Peak-Fitting Routine

XRD patterns were analyzed using a custom peak fitting routine in Igor Pro, which can be found at https://github.com/allisonmis/IgorPeakFit.

A window around the expected location of each peak was defined; peaks were then located and fit to pseudo-Voigt curves, and a cubic function was added to account for any background signal, as shown in Figure 1. This fitting routine cycled through each sample in a library, yielding peak height, width, and location for each diffraction peak at a variety of compositions.

If, for a particular sample, a peak was not detected at the expected location, its width and height were reported as null. For samples that displayed a broad amorphous signal instead of crystalline peaks, that curve was fitted with a pseudo-Voigt but the returned width of that peak was anomalously large, (*e.g.*, greater than 5 degrees 2θ) which allowed it to be filtered from the crystalline data set. Residuals for this fitting method usually averaged below 1% for a library, occasionally with larger ($\sim$5%) residuals at the peak maxima, likely due to sampling effects from the diffractometer detector. This generalized automated fitting method may be useful for other analyses in which peak width, height, and position can provide rapid information about material qualities.

Uses for Values Returned by the Peak-Fitting Routine

Information gathered from this fitting approach includes the amorphous background function and peak height, width, and location.

The cubic function used to fit to the background was chosen solely for ease of fitting and does not have any easily-interpretable correlation with the amount or type of amorphous material in the
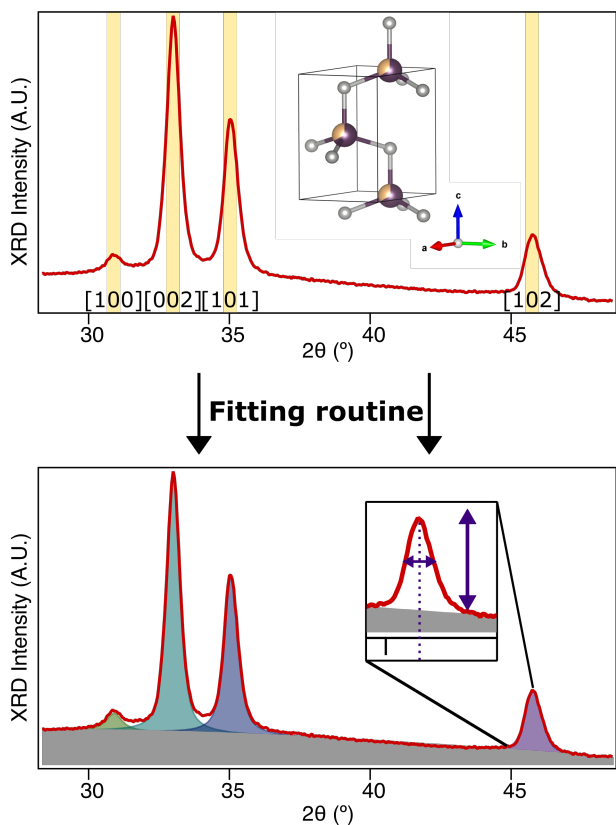
Fig. 1 Top: an XRD pattern with expected peak locations highlighted in yellow. These regions are defined and labeled by the user. Inset is the wurtzite cell of disordered Zn_2SbN_3. Bottom: the fit produced by the fitting routine consists of a cubic background (gray) and individual pseudo-Voigt peaks for each peak of interest (colors). The location, width, and height of each of these peaks are extracted (inset).

films. The overall area of the background function was found to vary with film thickness and x-ray tube age, and was thus not a useful parameter to track.

Diffraction peak height is dependent on a number of factors—film thickness, film texturing, x-ray source intensity, and detector integration time, among others—and accounting for all of these factors is more laborious than the intended high-throughput use case. As such, peak height comparison between libraries was not performed, though comparison of different index peaks within the same library may be illuminating, as the XRD scans on a particular library are acquired sequentially. As shown in Figure S1, thin-film texturing in this material varies somewhat with composition. The [002] peak is the strongest and thus was the primary peak used for the analysis below; the proposed crystalline regime of the film was not significantly altered by including or excluding the [100], [101], and [102] peaks.

This analysis uses peak full-width at half-maximum (FWHM) as a rough indicator of crystallite size; all non-synchrotron diffraction scans were performed on the same equipment with identical settings to remove variation in FWHM due to instrumental contributions. Crystalline material with large grains will yield narrow diffraction peaks, thus a low FWHM is indicative of crystalline material with large grains. These are the most relevant metrics for high-level materials discovery, thus in this paper we use low

FWHM as a crude indicator that a sample is high enough quality to warrant future investigation. Further discussion of FWHM values can be found in later sections of this work.

Diffraction peak location, which is dependent on atomic spacing and therefore has the potential to indicate solid solubility and/or defect-induced lattice expansion or contraction, has been shown to shift with varying composition in combinatorial studies of other materials.[16,17] The above peak-fitting process, when implemented on Zn_2SbN_3, yielded uncertainties for peak center values that were large enough to obscure any trend with composition, so these peak location values were not used to extract information about variations in lattice parameters. Instead, Pawley refinements were used on a set of growths downsampled using the peak fitting FWHM values. Further discussion of these Pawley refinements can be found in the section of this work on off-stoichiometry.

2 Results and Discussion

Growth Parameter Space of Zn_2SbN_3

Initial growth of the film followed previously-reported[5] growth conditions for this material. Only one growth parameter was altered at a time. Substrate temperature, chamber pressure, gun-substrate distance, working gas ratio, and total gun power were all studied independently. For each growth parameter, libraries were grown at varying parameter values, and the FWHM values of those libraries were extracted using the automated routine described above.

Figure 2 shows an example FWHM vs. cation composition plot
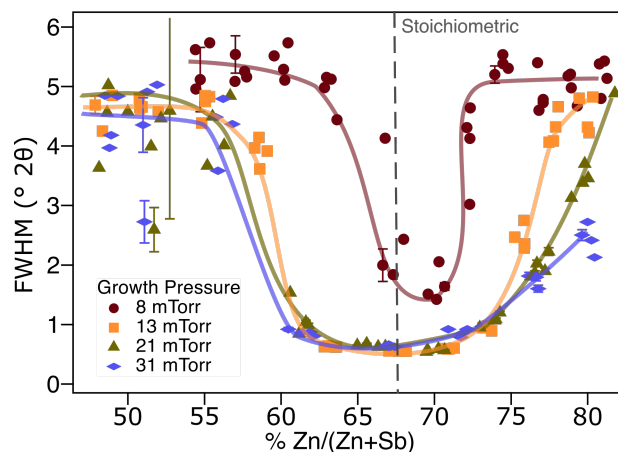

Fig. 2 FWHM of the [002] peak versus cation composition for various growth pressures with a line to indicate the stoichiometric composition. The 8 mTorr growth displays a higher FWHM throughout, indicating that this material is of lower crystalline quality than those from the other growth pressures. Among the higher growth pressures, there is little difference in minimum FWHM value or the composition range of the crystalline regime, indicating that these conditions produce roughly equivalent film quality. Lines are shown as guides to the eye and do not represent a fit.

for four different growth pressures. Lowest FWHM values, corresponding to large crystallites, occur around the stoichiometric composition (dashed vertical line). For most samples, a basin in FWHM values is seen across roughly 60-75 cation% Zn, (*i.e.*,

$\%\frac{Zn}{Zn+Sb}$) however the FWHM minimum for the 8 mTorr sample is neither as low nor as wide. From this plot, we conclude that 13 mTorr is a lower bound on effective growth pressure, but above that pressure there is little difference in film crystallinity up to 31 mTorr. Not shown in this plot is the secondary phase of metallic Sb observed in the 31 mTorr sample; further discussion of this secondary phase can be found in the section on nitrogen activation.

A similar process was followed for the other growth conditions studied with similar results: some parameter settings resulted in amorphous or low quality films, but most films had near-identical minimum FWHM values and crystallinity composition ranges (See Figures 3 and S2-S4). Beamline data plotted in Figure S5, for which the instrumental broadening is much less than for a lab diffractometer, show that the minimum FWHM values obtained using the Bruker diffractometer represent a true minimum FWHM, not an instrumental limit.

From this, we conclude that crystalline Zn_2SbN_3 will grow under a wide variety of conditions, and within that crystalline regime there is little relationship between crystallite size and growth parameters. While it is encouraging from an applications standpoint that the crystallinity of Zn_2SbN_3 is robust across varied growth conditions, this does not necessarily imply that electrical or optical properties are similarly unaffected. Table 1 lists the boundaries for each growth condition studied, along with additional insights discussed later in this work.

Exploring Off-Stoichiometry

As discussed above, within the growth space that produces crystalline material, the variation of growth parameters yields little difference in XRD peak sharpness and the composition range over which Zn_2SbN_3 is crystalline. The exception to this is substrate temperature, for which a FWHM vs. cation composition plot can be seen in Figure 3.

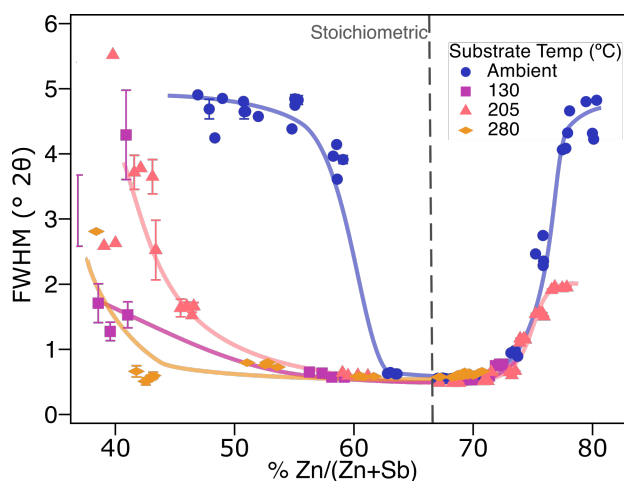The sample for which there is no intentional substrate heating

Fig. 3 FWHM of the 002 peak versus cation composition for various substrate temperatures during growth. Samples grown with intentional substrate heating show much wider crystallinity basins. Lines are shown as guides to the eye and do not represent a fit.

displays a much narrower crystalline composition range, while samples grown at elevated substrate temperatures are crystalline by XRD below 50 cation% Zn. No other growth parameter examined showed such a marked extension of off-stoichiometric crystallinity or produced films that were crystalline below 55 cation% Zn. Data from heavily zinc-rich samples are not available for high-temperature films due to the high vapor pressure of Zn and subsequent desorption from the film.

Cross-sectional microscopy of varying compositions in the film grown at 280 ° C, shown in Figure 4, revealed an explanation for the crystallinity of heavily Sb-rich material: an amorphous layer atop the crystalline film. EDS mapping showed this layer to be rich in antimony and oxygen. Both the amorphous and crystalline layers are included in the sampling volume of the XRF measurements used to determine film composition, resulting in Sb-rich composition values that do not represent the composition of the crystalline material. The background of the XRD peak fitting function was too variable to be of use in detecting this secondary amorphous layer with XRD alone.

EDS quantification was used to further examine these regions; first a composition of the entire film thickness, combining all phases present, was calculated and verified against XRF measurements. Next, if a sample was multi-phase, spatial boundaries were drawn to isolate the phases and the EDS spectra within each boundary were analyzed to yield phase-specific compositions.

The near-stoichiometric and Zn-rich regions (69.7 ± 3.4 and 71.6 ± 3.8 cation% Zn by EDS, respectively) both appear to be single-phase and without elemental segregation.

However, at even slightly Sb-rich conditions (64 ± 3.3 cation% Zn by EDS when including the whole thickness of the film) pockets of Sb-rich amorphous material are apparent at the surface of the film. The crystalline region of this film has a composition of 67.6 ± 3.3 cation% Zn.

The most overall Sb-rich sample studied (56.9 ± 3.2 cation% Zn by EDS when including the whole thickness of the film) has the most visible crystalline/amorphous segregation. The crystalline layer has a composition of 66.3 ± 3.3 cation% Zn by EDS. This proves that though we see crystalline XRD signal in Sb-rich regions of the film, the crystalline material itself in these regions is not Sb-rich. In fact, while crystalline Zn_2SbN_3 can accommodate excess Zn, the crystalline layers in these Sb-rich regions are near-stoichiometric, indicating that the solubility of excess Sb in Zn_2SbN_3 is very low.

Also visible in this micrograph are crystalline protrusions into the amorphous region; these protrusions have a similar composition to the crystalline layer. These protrusions indicate that the segregation of excess Sb from the crystal likely occurs during growth. The Sb layer is likely oxidized upon removal from the chamber. As this extension of crystalline material into Sb-rich areas of the film has only been observed on films grown at elevated temperatures, it is proposed that growth at elevated temperatures provides the energy necessary for crystallization at the substrate surface. The crystalline layer does not accommodate excess Sb, so as the material crystallizes, the excess Sb is pushed to the top of the film.

These structures are reminiscent of vapor-liquid-solid (VLS) growth, in which vapor preferentially deposits on a liquid alloy

Table 1 The growth parameters studied in this work and the values that result in crystalline material. Additional FWHM vs Composition graphs can be found in the supplemental information

Parameter	Optimized Value
Growth temperature	Crystalline layer in Sb-rich regions >100°C; film does not deposit >280°C
Gun-substrate distance	Closer yields a slightly wider crystalline region
Growth pressure	Not a large difference >10 mTorr; potential for secondary Sb phase >20 mTorr
Total gun power	Slower growth yields a slightly wider crystalline region
Ar:N_2 Ratio	5:15 sccm Ar:N_2 is highest Ar content that is still crystalline

on the substrate, and crystalline material precipitates out of the alloy, or flux growth, in which crystalline material precipitates out of a molten flux. It may be that for Sb-rich growth conditions, deposited material behaves similarly to the flux or VLS alloy: stoichiometric material precipitates onto the substrate, forming a crystalline layer, and a Sb-rich layer is left on top. As more material is deposited, it goes into solution in this layer, and then some of it is precipitated out onto the existing crystallites, growing the layer of crystalline material and the layer of excess Sb on top. In a scenario with excess Zn, the Zn incorporates into the crystalline material instead of accumulating on top of the active growth layer, so no Zn segregation is observed.

Antimony has been used for decades as a surfactant during molecular beam epitaxy[18] (MBE) and metal organic vapor phase epitaxy[19] (MOVPE) growth of high-quality semiconductors due to its ability to change surface thermodynamics and kinetics. Given this behavior in other growth systems, it is plausible that Sb plays a similar role in the sputter growth of Zn_2SbN_3: a surface layer that mediates crystal growth.

The images in Figure 4 come from a single library grown at 280°C. Pawley refinements were carried out on the rest of the temperature series to examine their off-stoichiometric behavior. A comparison of lattice parameter values for off-stoichiometric Zn_2SbN_3 and other Zinc-based ternary nitrides, $ZnGeN_2$ and $ZnSnN_2$ is shown in Figure 5. The ionic radii[20] of Ge^{4+}, Sb^{5+}, Sn^{4+}, and Zn^{2+} (67, 74, 83, and 88pm, respectively) may lead one to expect that the lattice parameters of the three nitride compounds would increase with increasing zinc content. While this trend holds true for $ZnGeN_2$,[17] cell size actually decreases with excess Zn in $ZnSnN_2$,[16] a phenomenon attributed to alloying with the smaller wurtzite cell of ZnO. Though the Zn_2SbN_3 films are grown without intentional oxygen content, target oxidation and residual water vapor in the growth chamber have been shown to contaminate nitride films grown under similar circumstances in this chamber 15% $\frac{O}{N+O}$ or more,[7,21] so oxygen contamination of these Zn_2SbN_3 films is likely.

As seen in Figure 5, there is not a clear trend that unites the Zn_2SbN_3 samples grown at varying temperatures, in contrast to $ZnSnN_2$ and $ZnGeN_2$. The films grown at 205°C and 280°C show downward trends similar to those seen in $ZnSnN_2$, indicating that excess Zn in high-temperature films may be accommodated by alloying with ZnO. The slight upward trend in the Zn-rich region of the film grown at 130°C may be an indication that for films grown at this intermediate temperature, excess Zn is incorporated into the lattice instead of alloying with ZnO. The films grown without intentional heating show no change in lattice parameter with Zn content, indicating that off-stoichiometry is not incorporated into

the lattice.

It is worth noting that the low-angle superlattice peaks associated with cation ordering were not observed at any composition for any growth conditions. Despite the fact that the ordered supercell is a lower-energy configuration than the disordered cell, it is not surprising that films grown without intentional substrate heating are cation-disordered: the cations are kinetically limited and cannot rearrange into an ordered pattern given the rapid growth rate associated with sputtering. At higher temperatures, the cations are no longer kinetically limited, and will form ordered material. As growth temperature increases, there is a thermodynamic transition[2] above which cation disorder is entropically favored and the material will become disordered.

Given that films did not grow when substrate temperatures were above 280°C, it is likely that this is roughly the decomposition temperature of Zn_2SbN_3. The lack of superlattice XRD peaks and the gradual absorption onset observed in this material (see Figure S6) indicate that the material grown was cation disordered, and that the temperature required to overcome kinetic limitations to ordering is above the decomposition temperature of Zn_2SbN_3.

This phenomenon may also offer an explanation for the accommodation of off-stoichiometry at low temperatures: the kinetic difficulties of ordering and the entropic benefits of antisite defects may allow for Zn_2SbN_3 to maintain its crystallinity for a small off-stoichiometric regime.

The Role of Nitrogen Activation in Film Quality

The wide stability range of Zn_2SbN_3 is somewhat surprising given its predicted metastable nature. In fact, the only growth conditions that resulted in films with no crystalline XRD peaks were high gun powers (17.8 $\frac{W}{in^2}$ total) and a high Ar:N_2 ratio. Gun power may affect multiple relevant thermodynamic and kinetic variables, but a simple explanation is that high gun powers lead to high deposition rates and that there is a deposition rate beyond which the deposited surface does not have adequate time to crystallize before a new surface has been deposited on top.

The growth of amorphous material at high Ar:N_2 ratios and fixed total gas flow may simply be due to the lower concentration of nitrogen in the growth environment. It may also be related to the metastable nature of Zn_2SbN_3, which needs an elevated μ_N to form. It may be the availability of activated nitrogen, not nitrogen in general, that is the limiting factor in the formation of crystalline material.

The exact source of the elevation in chemical potential is not well understood; it is likely due to a combination of unintentional N_2 activation through interaction with the sputter plasmas and intentional N_2 activation through a plasma source. It is unclear
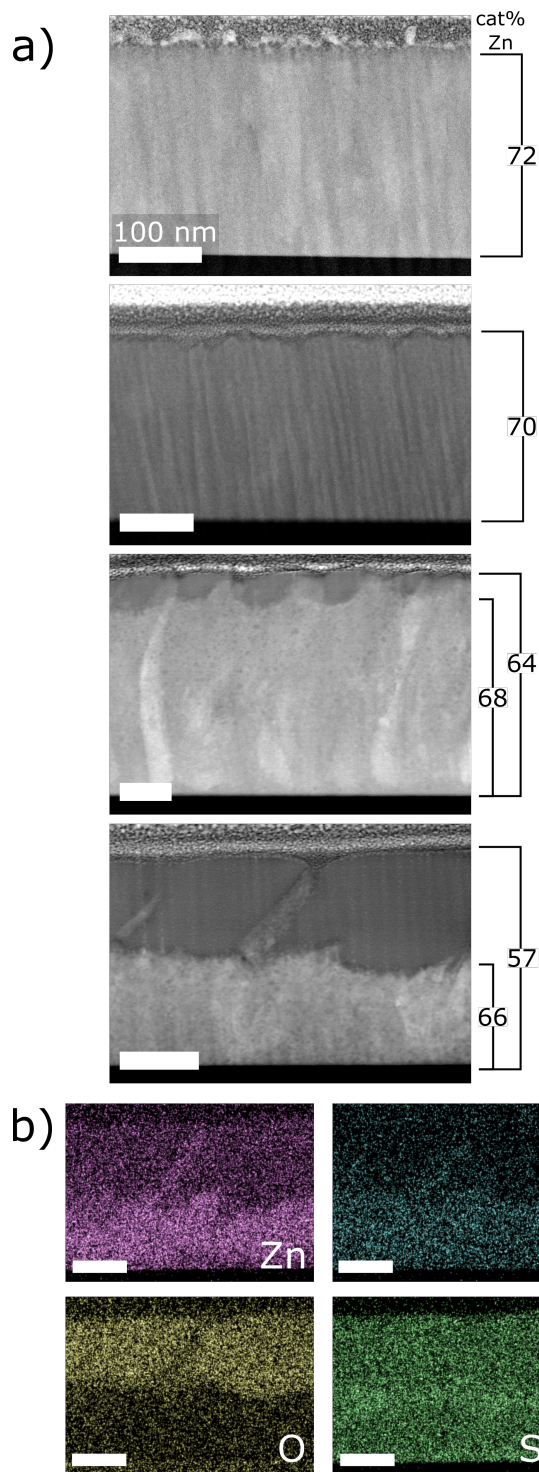
Fig. 5 The *a* lattice parameter plotted against cation compositon for films grown at multiple temperatures. Literature values for *a* for $ZnGeN_2$/ and $ZeSnN_2$ are plotted alongside for comparison.[16,17] The 130°C film shows a slight upward trend in *a* with increasing Zn, though weaker than $ZnGeN_2$. The 280°C and 205°C films show slight downward trends with increasing Zn similar to $ZnSnN_2$. $ZnGeN_2$ and $ZnSnN_2$ are plotted on a separate x-axis due to their stoichiometry, and $ZnGeN_2$ is plotted on its own y-axis to allow for readable y scaling.

Fig. 4 a)Cross-sectional HAADF STEM images of varying compositions from a single library grown at 280°C. EDS-derived cation compositions are listed for whole film thickness and crystalline regions. b) Element mapping of the 57 cation% Zn film shows that the amorphous top layer is O-rich and Zn- and N-poor.

what proportion of the N_2 present is activated enough to form crystalline material, but a high Ar:N_2 ratio likely decreases the concentration of activated nitrogen.

To further probe the relationship between crystallinity and nitrogen supply, several films were grown without the use of the ECR
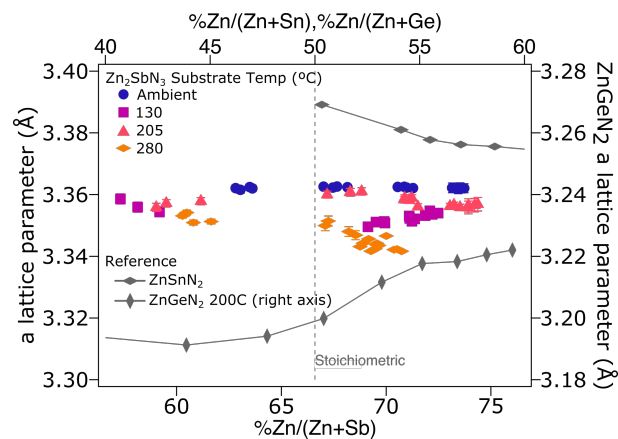
plasma source but with all other parameters nominally identical to those of prior growths. Nitrogen was flowed into the chamber through the ECR outlet, but was not intentionally activated. The resultant films were similar in appearance and crystallinity to those grown with ECR-activated nitrogen, except for those grown above 13 mTorr of total chamber pressure. These films grown at higher pressure and without intentionally-activated nitrogen showed a secondary phase in XRD that proved to be metallic antimony in a trigonal $R\bar{3}m$ phase. The XRD patterns of two full libraries, plotted with composition on the y axis and x-ray intensity on the color axis, are shown in Figure 6. The antimony phase exists across the entire composition range of the film, even at compositions outside the crystalline window for Zn_2SbN_3.

The growths without intentionally-activated nitrogen show that the energetic environment in a sputter growth chamber alone raises μ_N enough to form Zn_2SbN_3, but without additional nitrogen activation, a secondary phase of metallic Sb is also energetically favorable. Cross-sectional microscopy of one of these two-phase regions, shown in Figure 7, reveals that the metallic Sb phase is confined to a layer on top of the Zn_2SbN_3 film.

The location of this layer adds further support to the theory that Sb acts as a mediating layer on top of the film. Given that formation of this metallic Sb layer is suppressed by the presence of activated nitrogen, it is likely that μ_N affects the way this layer behaves, and whether it accumulates on the surface or incorporates into the rest of the film.

Computational Insights Into Ordering

The material properties reported by Arca, *et al.*[5] disagreed somewhat with calculated properties: the optical absorption curve was less steep and occurred at a lower energy than calculated, and
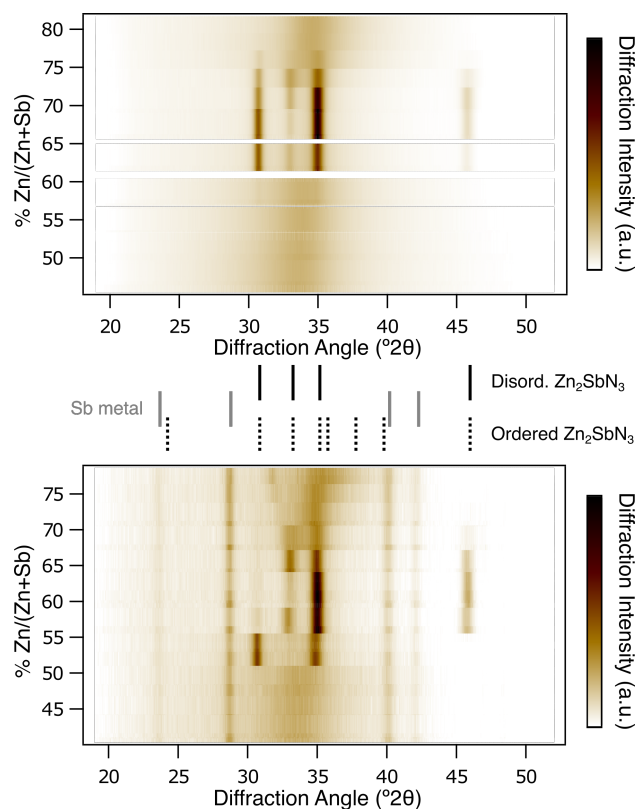
Fig. 6 XRD patterns for two libraries, plotted as a function of cation composition. These films were grown under identical conditions except the top library was grown with intentionally-activated nitrogen, while there was no intentional activation for the bottom library. Each horizontal row contains a 1D XRD plot; peak intensities are represented by darker areas. The top plot (activated nitrogen) is single-phase Zn_2SbN_3 where crystalline and amorphous elsewhere. The bottom plot (no intentional N activation) has the addition of a metallic Sb phase throughout all compositions. XRD reference peak locations can be seen between plots.
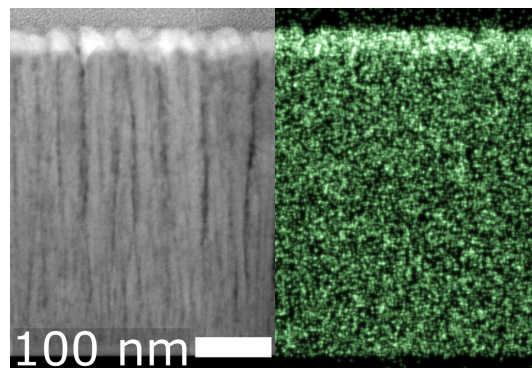

Fig. 7 Cross-sectional STEM HAADF of a two-phase region of a film grown without intentional nitrogen activation (left) and an element map of Sb. The secondary phase of Sb metal resides as a top layer on the crystalline Zn_2SbN_3 film below.

the bandgap energy as determined by photoluminesence was 0.2 eV lower than predicted. These discrepancies were attributed to the material being cation-disordered, while the predicted properties all assumed cation ordering. Absorption measurements performed on these films behaved similarly (see Figure S6). A clearer understanding of the nature of cation ordering in Zn_2SbN_3 was needed to evaluate whether ordering, and thus the theoretical absorption behavior, can be achieved.

In the ground state, cation ordering lowers the symmetry relative to the average wurtzite structure of the disordered ternary nitrides. In $ZnSnN_2$ and $ZnGeN_2$, Monte-Carlo (MC) simulations have provided detailed insights into both short- and long-range order (SRO and LRO) changes associated with the order-disorder transition.[15,22] While MC simulations are not yet available for Zn_2SbN_3, we can analyze the crystal structure predictions from Ref. 4 to derive some insights on the ordering behavior of Zn_2SbN_3 and the resulting impact on the electronic properties. In Ref 4, the crystal structures were found using the kinetically limited minimization (KLM) method, which is a hybrid approach combining elements of both random and basin-hopping structure searches.[23] A key feature of the KLM approach is the enforcement of suitable pairwise minimum interatomic distances, which re-

duces the configuration space and greatly enhances the efficiency of the search.[23] We used 2.0 Å as minimum distance for the nearest neighbor and 3.0 Å for the next nearest neighbor pairs, except for the N-N pair where a slightly smaller threshold of 2.9 Å was used. Incorporating these constraints, over 400 initial seed structures in 12 atom unit cells were generated. Out of these, the space group (sg) 36 ground state was obtained with a rate of about 5%, and almost half of the initial seeds resulted in one of the 7 low energy structures.

Using the kinetically limited minimization (KLM) approach[6,23] and a 12-atom sampling cell size, a total of 7 non-equivalent crystal structures were found within an energy window of 50 meV/cation (meV/cat) with respect to the ground state. All of them have similar local ordering: the nitrogen atoms are 4-fold coordinated with a 2:1 ratio of N-Zn_3Sb_1 and N-Zn_2Sb_2 motifs. Structures with other motifs such as N-Zn_4 were found only at much higher energies, i.e., above 150 meV/cat.

Figure 8 shows the simulated XRD pattern for these 7 low-energy structures, identified by their respective space group number. The two lowest energy structures (sg 36 and 9) are wurtzite (WZ) derived, followed by 4 zinc-blende (ZB) derived structures and a second sg 36 WZ structure (labeled 36*). For comparison, Figure 8 also shows reference patterns for average WZ and ZB structures in which Zn and Sb occupy a single cation site in a 2:1 ratio. These structures were generated assuming the same atomic volume as the ground state (sg 36) and an average c/a ratio and u parameter for the WZ case. The average structures approximate the XRD signature of cation-disordered Zn_2SbN_3. The cation ordering in the KLM sampled structures causes superstructure peaks in the XRD (below 30 degrees), but there is notably no discernible splitting of the WZ or ZB principal peaks. Due to the similar atomic sizes of Zn^{2+} and Sb^{5+}, the shape of the WZ or ZB supercells remains nearly ideal. The absence of superstructure peaks in the experimental data suggests that the material is disordered and thus the electronic electronic structure is likely different than predicted.

It is instructive to consider $ZnSnN_2$ and $ZnGeN_2$ for comparison, which are both single motif phases (N-Zn_2Sn_2 and N-Zn_2Ge_2) but differ in their sensitivity to LRO. The two ideal-motif structures that are accommodated in small unit cells (the sg 33 ground state
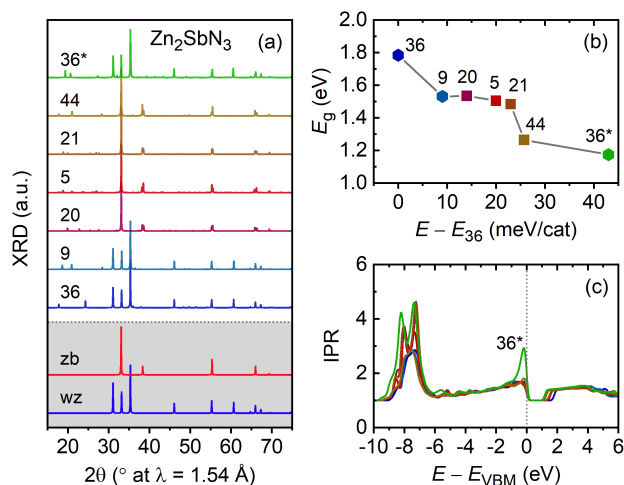
Fig. 8 (a) Simulated XRD patterns for the 7 lowest energy structures of Zn_2SbN_3 found by KLM structure prediction.[4] The different structures are labeled by the respective space group number, and reference patterns for average wurtzite and zinc-blende structures are shown at the bottom. (b) Dependence of the band gap energy as function of the structural total energy relative to the sg 36 ground state. (c) The inverse participation ratio, measuring carrier localization effects, as function of the electronic energy.

with a 16 atom primitive cell and a sg 26 structure with a 8 atom cell)[24] are virtually degenerate in energy in $ZnSnN_2$ ($\Delta E = 2$ meV/cat), but the energy difference is much larger in $ZnGeN_2$ ($\Delta E = 54$ meV/cat). This sensitivity is also reflected in the electronic properties, where the band gap of the sg 26 structure is reduced relative to sg 33 by merely 0.04 eV in $ZnSnN_2$, but by as much as 0.52 eV in $ZnGeN_2$. As seen in Figure 8, the behavior of Zn_2SbN_3 falls somewhere in between that of the two Zn-IV nitrides. The first structure above the ground state has an energy of $\Delta E = 9$ meV/cat, and the band gap is reduced by 0.25 eV. The figure also shows the general trend of decreasing band gaps with increasing structural energies. Assuming that the structure of disordered samples reflects a mixture of the ordering patterns of the different WZ structures obtained from structure sampling, we can expect a moderate band gap reduction in disordered Zn_2SbN_3, which would help to explain the observation of a somewhat smaller than expected band gap ($E_g = 1.55$ eV from PL vs 1.71 eV from GW calculation, Ref. 5).

As a measure of carrier localization effects, we further calculated the inverse participation ratio (IPR) from the local density of states (see 15 for details), shown in Figure 8c. With exception of the highest energy sg 36*, all structures show delocalized behavior with IPR < 2 in the vicinity of the band edges, which should be conducive to good semiconducting properties (IPR = 1 would indicate perfect delocalization). A notable feature of the sg 36* structure is that all Zn and Sb atoms are arranged in 1 dimensional chains, which is possibly the origin of the stronger localization effects (IPR = 3) in this structure close to the valence band maximum (Figure 8c). However, this highly ordered feature should not be prevalent in disordered structures. Finally, the ZB-derived structures seem to blend in with the WZ structures in the trends of energies, band gaps, and carrier localization (Figure 8

b and c), suggesting the possibility of low-energy stacking faults. The experimental data above does not provide evidence for any stacking faults, but our computational results suggest that they might have benign properties if they were to occur.

3 Conclusions and Outlook

Zn_2SbN_3 is one of many predicated novel ternary nitrides with promising optoelectronic properties. The material was first realized in Reference 5, and it was shown to have room temperature photoluminesence and a conduction band minimum well-aligned for hydrogen evolution reactions. In this work, this promising material was further evaluated.

The effect of off-stoichiometry and deposition parameters on crystallinity of the novel material Zn_2SbN_3 was explored using high-throughput combinatorial thin film growth. Crystallinity was assessed by examining the FWHM of XRD measurements taken at a variety of compositions for each growth condition. Narrower peaks indicate larger crystallite size and thus growth/composition regimes worth pursuing for future exploration of this material. Zn_2SbN_3 was found to crystallize under a wide range of growth conditions, and within those crystalline-producing conditions there was little dependence of crystallite size on the exact settings of the growth conditions themselves.

The use of intentionally-activated nitrogen is helpful for suppressing a secondary phase of metallic Sb, especially at higher chamber pressures. Samples grown at higher substrate temperatures showed segregation of crystalline material from excess Sb within heavily Sb-rich regions of the film. The crystalline layers in these regions were near-stoichiometric. Zn-rich regions of the film showed no signs of elemental segregation, indicating that this material accommodates excess Zn in the lattice to a greater degree than excess Sb. Growth pressure and temperature phase diagrams based on the data in this work can be found in Figures S7 and S8.

The potential for secondary phases in Sb-rich material limits the range of potential composition-based property tuning in Zn_2SbN_3 to stoichiometric and Zn-rich compositions only. The proposed surfactant behavior of Sb during growth may enable the growth of novel geometries like nanowires or be used to remove impurities and thus improve material quality.

Computational efforts have concluded that there are multiple ordered supercells of the same stoichiometry with comparable energies of formation. This energetic proximity suggest that long-range disorder can develop readily, and perhaps will be unavoidable under the kinetic conditions of the synthesis process. However, these structures retain the same short range order (N coordination motifs) as the ground state, and the effect of disorder on the electronic properties – apart from a moderate band gap reduction - are expected to be benign. No superlattice diffraction peaks were observed for any growth conditions studied here, and the observed gradual absorption onset and low absorption onset energy indicate that this material is likely disordered.

Further study of this material is needed to assess what effect growth conditions have on material performance in devices. Of particular interest is the long-term stability of Zn_2SbN_3; its metastable nature may make it prone to degradation, though

Cu_3N, another metastable nitride, has been shown to have a shelf life of over a year.[25] The optical properties described in Reference 5 show that stoichiometric Zn_2SbN_3 has promise for device applications, but the results described in this work indicate that ordering-based and composition-based tunability are limited for this material.

Conflicts of interest

There are no conflicts to declare.

Acknowledgements

Notes and references

1 A. L. Greenaway, C. L. Melamed, M. B. Tellekamp, R. Woods-Robinson, E. S. Toberer, J. R. Neilson and A. C. Tamboli, *Annual Review of Materials Research*, 2021, **51**, 591–618.

2 R. R. Schnepf, J. J. Cordell, M. B. Tellekamp, C. L. Melamed, A. L. Greenaway, A. Mis, G. L. Brennecka, S. Christensen, G. J. Tucker, E. S. Toberer, S. Lany, A. C. Tamboli and A. C. Tamboli, *ACS Energy Letters*, 2020, **5**, 2027–2041.

3 A. D. Martinez, A. N. Fioretti, E. S. Toberer and A. C. Tamboli, *J. Mater. Chem. A*, 2017, **5**, 11418–11435.

4 W. Sun, C. J. Bartel, E. Arca, S. R. Bauers, B. Matthews, B. Orvañanos, B. R. Chen, M. F. Toney, L. T. Schelhas, W. Tumas, J. Tate, A. Zakutayev, S. Lany, A. M. Holder and G. Ceder, *Nature Materials*, 2019, **18**, 732–739.

5 E. Arca, J. D. Perkins, S. Lany, A. Mis, B.-R. Chen, P. Dippo, J. L. Partridge, W. Sun, A. Holder, A. C. Tamboli, M. F. Toney, L. T. Schelhas, G. Ceder, W. Tumas, G. Teeter and A. Zakutayev, *Mater. Horiz.*, 2019, **6**, 1669–1674.

6 E. Arca, S. Lany, J. D. Perkins, C. Bartel, J. Mangum, W. Sun, A. Holder, G. Ceder, B. Gorman, G. Teeter, W. Tumas and A. Zakutayev, *Journal of the American Chemical Society*, 2018, **140**, 4293–4301.

7 A. L. Greenaway, A. L. Loutris, K. N. Heinselman, C. L. Melamed, R. R. Schnepf, M. B. Tellekamp, R. Woods-Robinson, R. Sherbondy, D. Bardgett, S. Bauers, A. Zakutayev, S. T. Christensen, S. Lany and A. C. Tamboli, *Journal of the American Chemical Society*, 2020.

8 K. R. Talley, S. R. Bauers, C. L. Melamed, M. C. Papac, K. N. Heinselman, I. Khan, D. M. Roberts, V. Jacobson, A. Mis, G. L. Brennecka, J. D. Perkins and A. Zakutayev, *ACS Combinatorial Science*, 2019, **21**, 537–547.

9 B. H. Toby and R. B. Von Dreele, *Journal of Applied Crystallography*, 2013, **46**, 544–549.

10 J. Sun, A. Ruzsinszky and J. P. Perdew, *Phys. Rev. Lett.*, 2015, **115**, 036402.

11 H. T. Stokes and D. M. Hatch, *Journal of Applied Crystallography*, 2005, **38**, 237–238.

12 G. Kresse and D. Joubert, *Phys. Rev. B*, 1999, **59**, 1758–1775.

13 J. Paier, R. Hirschl, M. Marsman and G. Kresse, *The Journal of Chemical Physics*, 2005, **122**, 234102.

14 S. Lany, H. Raebiger and A. Zunger, *Phys. Rev. B*, 2008, **77**, 241201.

15 S. Lany, A. N. Fioretti, P. P. Zawadzki, L. T. Schelhas, E. S. Toberer, A. Zakutayev and A. C. Tamboli, *Phys. Rev. Materials*, 2017, **1**, 035401.

16 A. N. Fioretti, J. Pan, B. R. Ortiz, C. L. Melamed, P. C. Dippo, L. T. Schelhas, J. D. Perkins, D. Kuciauskas, S. Lany, A. Zakutayev, E. S. Toberer and A. C. Tamboli, *Materials Horizons*, 2018, **5**, 823–830.

17 C. L. Melamed, J. Pan, A. Mis, K. Heinselman, R. R. Schnepf, R. Woods-Robinson, J. J. Cordell, S. Lany, E. S. Toberer and A. C. Tamboli, *Journal of Materials Chemistry C*, 2020, **8**, 8736–8746.

18 C. W. Pei, B. Turk, J. B. Héroux and W. I. Wang, *Journal of Vacuum Science & Technology B: Microelectronics and Nanometer Structures Processing, Measurement, and Phenomena*, 2001, **19**, 1426–1428.

19 L. Zhang, H. F. Tang, J. Schieke, M. Mavrikakis and T. F. Kuech, *Journal of Applied Physics*, 2002, **92**, 2304–2309.

20 R. D. Shannon, *Acta Crystallographica Section A*, 1976, **32**, 751–767.

21 C. L. Melamed, M. B. Tellekamp, J. S. Mangum, J. D. Perkins, P. Dippo, E. S. Toberer and A. C. Tamboli, *Physical Review Materials*, 2019, **3**, 1–7.

22 J. J. Cordell, J. Pan, A. C. Tamboli, G. J. Tucker and S. Lany, *Phys. Rev. Materials*, 2021, **5**, 024604.

23 A. Sharan and S. Lany, *The Journal of Chemical Physics*, 2021, **154**, 234706.

24 P. C. Quayle, E. W. Blanton, A. Punya, G. T. Junno, K. He, L. Han, H. Zhao, J. Shan, W. R. L. Lambrecht and K. Kash, *Phys. Rev. B*, 2015, **91**, 205207.

25 C. M. Caskey, R. M. Richards, D. S. Ginley and A. Zakutayev, *Materials Horizons*, 2014, **1**, 424–430.